RSC Advances

PAPER

View Article Online
View Journal | View Issue

Cite this: *RSC Adv.*, 2026, **16**, 15266

Optical response and electron energy loss spectra of boron arsenide using linear response theory

Nikhil Joshi, Shruti Jangir and K. B. Joshi *

In this study, we present optical and electron energy loss spectra of BAs using linear response time-dependent density functional theory. The spectra show the effects of local field and electron–hole interactions. The excitonic effects are included by considering the long-range-corrected and bootstrap exchange–correlation kernels. When the optical spectra from the long-range corrected and bootstrap kernels are compared with those from random phase approximation and adiabatic local density approximation, clear signatures of electron–hole interactions are observed. The current study marks the presence of continuum excitonic effects. The exciton binding energies of 38 and 44 meV deduced from long-range-corrected and bootstrap kernels using the hydrogenic model, respectively, are very close to the data obtained from GW–Bethe–Salpeter equation. It is found that the local-field effects reduce whereas electron–hole interactions enhance the high-frequency dielectric constant. Moreover, a clear modification in the electron energy loss spectra is visible after incorporating the local-field effect. We discuss the effect of the material-dependent parameter α, deduced from a number of approaches, on both optical and electron energy loss spectra. This study corroborates the effectiveness of long-range-corrected kernel in exploring the optical and electronic spectra when α evaluated using the scheme developed by the authors is considered.

Received 7th February 2026
Accepted 26th February 2026

DOI: 10.1039/d6ra01107a

rsc.li/rsc-advances

1. Introduction

The last few years have witnessed the revival of research interest in boron compounds. This is attributed to the technological importance of these compounds in high-temperature, electronic and optical applications. Among the boron compounds, boron arsenide (BAs), crystallizing in the zinc blende (zb) structure, is an attractive material because of its high thermal conductivity and similarity of its band structure with Si to a large extent. Due to its high thermal conductivity, it has become important for efficient heat dissipation in microelectronic applications. In addition, BAs is of particular interest because of its highly covalent nature. Furthermore, due to the small core size and lack of p electrons in B, boron compounds display unusual dielectric behavior compared with other III–V and II–VI compounds.

Lindsay and Feng *et al.* independently reported the ultrahigh thermal conductivity (κ) of cubic BAs crystals using the first-principles method.[1,2] In experimental studies, major breakthroughs were achieved by growing high-quality cubic BAs crystals by three research groups.[3–5] However, discrepancies between the predicted and measured values of κ inspired researchers to study this material further.

The above studies were focused on high-temperature applications and thermal conductivity. Notably, B and As have similar order of electronegativity; hence, this simple compound is likely to have intriguing bonding and optical properties. Such studies on BAs began in the early seventies. A number of theoretical studies have been performed to examine the physical properties of cubic BAs; however, only a few of them have been devoted to the study of optical properties.[6–38] Recently, Barboza *et al.* investigated the effects of hydrostatic pressure on the electronic, excitonic, and optical properties of zb BAs using first-principles methods combined with a maximally localized Wannier function tight-binding model and the Bethe–Salpeter equation (BSE) formalism.[38] Acharya *et al.* reported the excitonic spectrum taking $\boldsymbol{q} = 0$ and finite $\boldsymbol{q}$. They observed bright optical transitions at 4 eV.[37] Bushick *et al.* determined the electronic and optical properties of BAs using density functional theory (DFT) and many-body perturbation theory (MBPT), including quasiparticle (QP) and spin–orbit coupling corrections.[28] Buckeridge and Scanlon computed the electronic band structure and optical properties using the relativistic QP self-consistent GW approach, including electron–hole (e–h) interactions through solution of the BSE.[30] Using first-principles methods, Bravić and Monserrat studied the role of temperature on the optoelectronic properties of BAs, considering electron–phonon interactions and thermal expansion.[31] The monolayer and h-BAs have also been investigated using first-

Department of Physics, Mohanlal Sukhadia University, Udaipur-313001, India. E-mail: cmsmlsu@gmail.com

principles methods to unravel the strain-dependent thermoelectric, electronic and optical properties.[39–41]

On the experimental side, Kang *et al.* measured refractive index using the Fabry–Pérot interference.[42] Song *et al.* systematically measured the optical properties of high-quality millimeter-sized BAs crystals using spectroscopic ellipsometry, transmission and reflection spectroscopy, together with DFT and MBPT, considering QP and excitonic corrections. The measured indirect and direct band gaps were found to be 2.02 and 4.12 eV, respectively.[43] Mahat *et al.* measured refractive index using the Brewster angle measurement technique.[44]

Excitons play an important role in describing the optical properties of materials.[45] The MBPT, using the GW approximation and the BSE, is generally employed to describe exciton-mediated optical properties.[46,47] Time-dependent density functional theory (TD-DFT) is also an efficient alternative approach.[48] It is highly effective for studying neutral excitations.[47,49] In this theory, the description of optical spectra depends essentially on the exchange–correlation (XC) kernel. To capture the excitonic effects, the kernel must behave as $1/q^2$ in the long-wavelength limit.[50,51] The most common approximations for the XC kernel are the random-phase approximation (RPA) and the adiabatic local density approximation (ALDA). In RPA, the XC kernel is zero,[52] whereas in the ALDA the XC kernel is local and static.[53,54] Both these approximations fail to capture excitonic effects due to their inability to capture the long-range behavior. Further, the long-range-corrected (LRC) kernel proposed by Reining *et al.*[55] and the bootstrap (BS) kernel proposed by Sharma *et al.*[56] accommodate the $1/q^2$ behavior. Hence, these are promising choices for the accurate description of the effect of excitons on the optical spectra within the TD-DFT.

The linear-response TD-DFT describes optical spectra very accurately in materials wherein intense e–h interaction is at work. The intense e–h interaction is characterized by the exciton binding energy varying from a few meV to about 100 meV *vis-à-vis* the continuum. The exciton binding energy in BAs is around 43 meV.[28] Some authors have reported that it lies within the 23–133 meV range.[28,38,57] The inadequate treatment of dielectric screening is found to be a major reason for variation in this estimate.[38] Nevertheless, these values signify that excitons are relatively stable against thermal dissociation at room temperature.

Very recently, the thermoelectric properties of BAs have been reported. This is found to be a p-type thermoelectric material.[6,41,58–62] The power factor of this compound shows low recombination; hence, the formation of e–h pairs is more probable. This is why the optical and electron energy loss spectra (EELS) of BAs are largely mediated by the e–h interaction. These features motivated us to select BAs for the investigations. Additionally, it is worth mentioning that Resta and Baldereschi have pointed out the intense local field effect (LFE) in ionic compounds, which has not been considered in earlier investigations.[63] It is recognized that the exciton oscillator strength is lower in covalent crystals and is not more than 10% of the oscillator strength of the NaCl-type ionic crystals.[64] Being covalent in nature, zb BAs offers a suitable electronic environment to examine the local field and excitonic effects. Very recently, an alternative approach, developed by the current authors to find the material-dependent parameter α required in the LRC kernel, delivered encouraging results on some zb and antifluorite crystals of ionic nature.[65–68] The α-parameter deduced this way accounts for the dielectric screening more effectively. This is why it would be interesting to apply this method to the covalent compound BAs.

Therefore, in this paper, a systematic study of the electronic and optical properties is undertaken, deploying advanced theoretical tools such as linear response TD-DFT. After settling the ground state, the dielectric properties, refractive indices and reflectivity are calculated and discussed. In addition, the EEL spectra are presented. Lastly, the effect of α, calculated by using our scheme, on the optical constants and EELS is analysed critically.

2. Methodology

2.1. Theory

In this section, we briefly summarize the methodology of linear response TD-DFT calculations. More details can be found in previous work.[65–67] The excited state calculations were performed within the linear response TD-DFT regime. In this theory, a Dyson-like equation for the density–density response function of the fully interacting system is given by:[69]

$$\chi\left(\boldsymbol{r},\boldsymbol{r}',t-t'\right)=\int_{-\infty}^{\infty}\mathrm{d}t''\int\mathrm{d}^3\boldsymbol{r}''\,\chi_{\mathrm{KS}}\left(\boldsymbol{r},\boldsymbol{r}'',t-t''\right)\Bigg[\delta\left(\boldsymbol{r}''-\boldsymbol{r}'\right)\delta\left(t''-t'\right)+\left\{\int_{-\infty}^{\infty}\mathrm{d}t'''\int\mathrm{d}^3\boldsymbol{r}'''\frac{\delta\left(t''-t'''\right)}{\left|\boldsymbol{r}''-\boldsymbol{r}'''\right|}\chi\left(\boldsymbol{r}''',\boldsymbol{r}',t'''-t'\right)\right\}+\left\{\int_{-\infty}^{\infty}\mathrm{d}t'''\int\mathrm{d}^3\boldsymbol{r}'''f_{\mathrm{XC}}\left(\boldsymbol{r}'',\boldsymbol{r}''',t''-t'''\right)\frac{\delta\rho\left(\boldsymbol{r}''',t'''\right)}{\delta v_{\mathrm{ext}}\left(\boldsymbol{r}',t'\right)}\right\}\Bigg],\quad(1)$$

where χ_{KS} is the linear density–density response function of the non-interacting Kohn–Sham (KS) system. The expression for the response function of interacting system in frequency space is:

$$\chi\left(\boldsymbol{r},\boldsymbol{r}',\omega\right)=\chi_{\mathrm{KS}}\left(\boldsymbol{r},\boldsymbol{r}',\omega\right)+\int\mathrm{d}^3\boldsymbol{r}''\int\mathrm{d}^3\boldsymbol{r}'''\chi_{\mathrm{KS}}\left(\boldsymbol{r},\boldsymbol{r}'',\omega\right)\left[\frac{1}{\left|\boldsymbol{r}''-\boldsymbol{r}'''\right|}+f_{\mathrm{XC}}\left(\boldsymbol{r}'',\boldsymbol{r}''',\omega\right)\right]\chi\left(\boldsymbol{r}''',\boldsymbol{r}',\omega\right),\quad(2)$$

where $f_{\mathrm{XC}}(\boldsymbol{r}'', \boldsymbol{r}''', \omega)$ is the XC kernel and is defined as:[70,71]

$$f_{\mathrm{xc}}\left(\boldsymbol{r}'',\boldsymbol{r}''',\omega\right)=\left.\frac{\delta v_{\mathrm{xc}}[\rho]\left(\boldsymbol{r}'',\omega\right)}{\delta\rho\left(\boldsymbol{r}''',\omega\right)}\right|_{\rho=\rho_{\mathrm{KS}}}.\quad(3)$$

In the current work, three choices for the f_{XC} are considered. In the ALDA the kernel is expressed as:[53,54,72]

$$f_{\mathrm{XC}}^{\text{TD-LDA}}\left(\boldsymbol{r},\boldsymbol{r}',t,t'\right)=\delta\left(\boldsymbol{r}-\boldsymbol{r}'\right)\frac{\mathrm{d}v_{\mathrm{XC}}^{\mathrm{LDA}}[\rho(\boldsymbol{r})]}{\mathrm{d}\rho(\boldsymbol{r})}\delta\left(t-t'\right).\quad(4)$$

Secondly, the LRC kernel developed by Reining *et al.* considers the long-range behavior adequately.[55] In crystals, the XC kernels covering long-range behavior in the limit $\boldsymbol{q} \to 0$ offer a few nice alternatives. The LRC is formulated to account for the long-range behavior in periodic solids. It has the form:[72–74]

$$f_{\mathrm{XC}}^{\mathrm{LRC}}\left(\boldsymbol{q}, \boldsymbol{G}, \boldsymbol{G}^{'}\right) = -\frac{\alpha}{\left|\boldsymbol{G}+\boldsymbol{q}\right|^{2}}\delta\left(\boldsymbol{G}-\boldsymbol{G}^{'}\right), \tag{5}$$

where α is a material-dependent parameter.

Thirdly, the parameter-free BS kernel developed by Sharma *et al.* has the form:[56,74]

$$f_{\mathrm{XC}}^{\mathrm{boot}}\left(\boldsymbol{q}, \boldsymbol{G}, \boldsymbol{G}^{'}, \omega\right) = \frac{\varepsilon^{-1}\left(\boldsymbol{q}, \boldsymbol{G}, \boldsymbol{G}^{'}, \omega=0\right)}{\chi_{\mathrm{KS}}\left(\boldsymbol{q}, \boldsymbol{G}=0, \boldsymbol{G}^{'}=0, \omega=0\right)}. \tag{6}$$

This kernel has the advantage that no system-dependent external parameter is required. Additionally, for comparison, we have also performed calculations using RPA, where $f_{\mathrm{XC}} = 0$.

In reciprocal space, the response function can be written as:[51]

$$\chi\left(\boldsymbol{G}, \boldsymbol{G}^{'}, \boldsymbol{q}, \omega\right) = \sum_{\boldsymbol{G}^{''}}\left\{\left[\delta(\boldsymbol{G}_1-\boldsymbol{G}_2) - \sum_{\boldsymbol{G}_3}\chi_{\mathrm{KS}}(\boldsymbol{G}_1, \boldsymbol{G}_3, \boldsymbol{q}, \omega)\times\left(\frac{4\pi\delta(\boldsymbol{G}_3-\boldsymbol{G}_2)}{\left|(\boldsymbol{G}_3+\boldsymbol{q})(\boldsymbol{G}_2+\boldsymbol{q})\right|} + f_{\mathrm{XC}}(\boldsymbol{G}_3, \boldsymbol{G}_2, \boldsymbol{q}, \omega)\right)\right]^{-1}\right\}_{\boldsymbol{G},\boldsymbol{G}^{''}} \chi_{\mathrm{KS}}\left(\boldsymbol{G}^{'}, \boldsymbol{G}^{''}, \boldsymbol{q}, \omega\right), \tag{7}$$

where $\boldsymbol{q}$ belongs to the first Brillouin zone (BZ) and $\boldsymbol{G}, \boldsymbol{G}'$ are the reciprocal lattice vectors. The χ thus deduced is a matrix. This equation can formally be written as:[75,76]

$$\chi = \chi_{\mathrm{KS}} + \chi_{\mathrm{KS}}(v + f_{\mathrm{XC}})\chi \tag{8}$$

or

$$\chi = \chi_{\mathrm{KS}}[1 - (v + f_{\mathrm{XC}})\chi_{\mathrm{KS}}]^{-1}. \tag{9}$$

Crystal LFE are contained within the Coulomb potential term v, which is a functional derivative of the Hartree potential with respect to density. If one includes only the long-range part of the Coulomb potential, $v_{\boldsymbol{G}=0}(\boldsymbol{q})$, then the microscopic response of the system to the external macroscopic field, the LFE, is neglected, and one only needs to calculate the head of the dielectric matrix, ε_{00}. However, if one includes the $\boldsymbol{G} \neq 0$ terms, then $\varepsilon_{\boldsymbol{G}\boldsymbol{G}'}$ is off-diagonal, and thus, matrix inversion has the effect of mixing the previously independent transitions.[77–79]

In reciprocal space, the inverse dielectric function can be written as:

$$\varepsilon^{-1}\left(\boldsymbol{G}, \boldsymbol{G}^{'}, \boldsymbol{q}, \omega\right) = \delta\left(\boldsymbol{G}-\boldsymbol{G}^{'}\right) + \sum_{\boldsymbol{G}^{''}}\frac{4\pi\delta\left(\boldsymbol{G}-\boldsymbol{G}^{''}\right)}{\left|(\boldsymbol{G}+\boldsymbol{q})\left(\boldsymbol{G}^{''}+\boldsymbol{q}\right)\right|}\chi\left(\boldsymbol{G}^{''}, \boldsymbol{G}^{'}, \boldsymbol{q}, \omega\right). \tag{10}$$

Thus, the inverse dielectric function follows directly from the response function. More often, the macroscopic dielectric function ε_{M} is also used to describe the optical spectra. This function is defined as:[79–81]

$$\varepsilon_{\mathrm{M}}(\omega) = \varepsilon_1 + i\varepsilon_2 = \lim_{q\to 0}\varepsilon_{\boldsymbol{G}=\boldsymbol{G}'=0}^{-1}(\boldsymbol{q}, \omega), \tag{11}$$

where the case $\boldsymbol{G} = \boldsymbol{G}' = 0$ delivers the head element of the $\varepsilon^{-1}(\boldsymbol{G}, \boldsymbol{G}', \boldsymbol{q}, \omega)$ matrix. Eqn (11) takes into account the crystal LFE because the dielectric matrix is inverted before the macroscopic average $\boldsymbol{G} = \boldsymbol{G}' = 0$ is taken.

The loss function $\mathcal{L}(\omega)$ that characterizes the EELS is given by:

$$\mathcal{L}(\omega) = -\mathrm{Im}\left\{\frac{1}{\varepsilon_{\mathrm{M}}(\omega)}\right\} = \frac{\varepsilon_2(\omega)}{\varepsilon_1{}^2(\omega) + \varepsilon_2{}^2(\omega)}. \tag{12}$$

The equation implies that the spectral features in EELS are given by regions where ε_2 has a peak corresponding to some interband transition, or ε_2 is very small and ε_1 vanishes. The latter condition determines the energy of the collective plasmon excitation.[82–85]

2.2. Alternative approach to find material-dependent parameter α in LRC

The empirical pseudopotential method (EPM) was originally developed to find electronic band structure from valence electrons of semiconductors and to study the reflectivity spectrum. The pseudopotential is constructed from a set of form factors (FFs). With advanced computational resources, one can refine the pseudopotential FFs. The refined sets of FFs have produced good results for the charge density, momentum density, elastic constants and reflectivity spectrum of several semiconducting compounds.[86,87] The FFs are available to construct the crystal potential with and without considering the *l*-dependent non-local effects for some IV, III–V and II–VI semiconductors.[86] In some cases, non-local pseudopotential methods have also been used to compute the momentum density distribution, which is compared with the experiment.[87] In general, the FFs considering *l*-dependent non-local effects give properties, such as momentum density, that better reconcile with experiments.

The excitonic physics within TD-DFT can be unfolded using the LRC kernel. However, as discussed earlier, it requires a material-dependent parameter α. A few methods have been suggested by a number of workers to find α.[72,73,76] The expression derived by Botti *et al.*[73] is:

$$\alpha = 4.615\varepsilon_{\infty}{}^{-1} - 0.213. \tag{13}$$

This relation contains the dielectric constant, which is a measure of the screening of the e–h interaction. The screening effect can also be captured by the polarity, defined by Vogl.[88] The polarity is related to the symmetric (V_S) and antisymmetric (V_A) FFs by the following formula:[88]

$$\alpha_p = -\frac{V_A(3)}{V_S(3)}. \quad (14)$$

One can use FFs to derive dynamic effective charges, elastic constants, and reflectivity spectra of a number of semiconducting compounds. Si and Ge are perfectly covalent semiconductors in the Vogl definition.[88] This amply recognizes that FFs also capture photon–lattice interactions, which is vital to describe the optical properties. Good quality optical spectra can be obtained using this FFs scheme if one chooses the finely tuned FFs for a compound. Therefore, this scheme is a good alternative to the method proposed by Botti *et al.* to capture the physics covered by α.[73]

Recently, efforts to relate the parameter α with FFs have also been made by Arruabarrena *et al.*[89] They introduced a non-negligible surface term and discussed its effect on the evaluation of exciton binding energy. The magnitude of this surface term for a few semiconductors is estimated using the Bloch functions derived from FFs proposed by Cohen–Bergstresser.[90]

3. Computational details

All calculations are performed by applying the full potential linearised augmented planewave (FP-LAPW) method.[91,92] Static DFT calculations are performed taking the local density approximation (LDA) proposed by Perdew and Zunger.[93] The muffin-tin radius for B and As was 1.64 Bohr and 2.18 Bohr, respectively. The plane wave cut–off parameter *rgkmax* was set to 7. The charge and energy self-consistent calculations were performed taking a Monkhorst–Pack (MP) net of 20 × 20 × 20 size.[94] To achieve self-consistency, Broyden mixing was considered.[95] The Murnaghan equation of state was fitted to the *E*–*V* data thus generated to deduce the equilibrium lattice constant, bulk modulus B_0, and the pressure derivative of the bulk modulus $B_0^{'}$.[96]

To find the response functions, many-body calculations are built on top of the ground state deduced from DFT at the LDA level. Since the optical calculations require a large number of *k*-points in the BZ, convergence with respect to this parameter was carefully achieved. The convergence test of the *k*-mesh size in the optical calculations reveals that an MP net of 128 × 128 × 128 size is sufficient. In the linear response TD-DFT calculations, ten empty states per spin per atom were included, and Gaussian-type smearing was applied, taking a width of 0.08 eV. The parameter *gmaxrf*, which is the maximum length of $\boldsymbol{G}$ vectors used in the calculation of the response function, was set to 3 atomic units (a.u.).

The scissor correction (SC) is a standard practice to correct the underestimation of the KS band gap resulting from the electronic structure calculations. This is well accepted when the optical properties of sp semiconductors and insulators are studied, since the optical spectra are largely determined by the bands around the Fermi level.[73] The use of this correction in the study of the optical spectra of semiconductors is corroborated by Arnaud and Alouani *et al.*[97] These authors point out that the difference between the calculated optical spectra using the GW quasiparticle energies, and the SC-corrected spectra is small for Si and a few other semiconductors. Application of SC is widely accepted by the community.[98,99] It causes a rigid shift (RS) to the optical and EEL spectra.[74,80] In the current work, SC or RS of 0.82 eV, arising from the difference between experimental and the LDA band gap, is applied.[43]

As mentioned earlier, RPA and three kernels, namely ALDA, LRC and BS, were examined. The LRC kernel requires a material parameter α, which can be deduced using three schemes. Firstly, the empirical relation proposed by Botti *et al.*[73] is used, which gives $\alpha = 0.29$. For this, the experimental value of the refractive index $n = 3.04$ is considered to find $\varepsilon_\infty = n^2$, which is equal to 9.242.[42] Secondly, the α values obtained from the FFs of X–As (X = Al, Ga, and In) series used in EPM are linearly interpolated; this gives $\alpha = 0.41$. Lastly, the symmetric and antisymmetric FFs used by Da Ng and Danner were taken to construct the local pseudopotential for BAs directly, which delivers $\alpha = 0.71$.[100]

4. Results and discussion

4.1. Structural and electronic properties

The structural properties obtained from the set of computational parameters given in the previous section are presented in Table 1. Results are in very good agreement with the experimental values. Other available results are also listed for comparison.

The band structure of the ground state derived using LDA is shown in Fig. 1(a). The most relevant region for the optical properties and interband transitions is highlighted in color. The figure depicts an indirect band gap of 1.11 eV. The minimum in the conduction band is towards the X point in the Γ to X direction. The direct excitation energies are: 3.30 eV at Γ, 4.72 eV at L, and 5.52 eV at X. Likewise, the direct energy gap between one band above the lowest conduction band and the top valence band at the L-point is 6.68 eV. All these characteristic energies are marked by up-down arrows and denoted by E_0, E_1, E_2 and $E_1^{'}$, respectively. The direct band gap is 3.30 eV. As expected for calculations at the LDA level, this is lower than the experimental value of 4.12 eV.[43]

Table 1 Lattice constant (*a*), bulk modulus (B_0), and the first derivative of bulk modulus ($B_0^{'}$) of zb BAs. Experimental data are taken from ref. 42

		Other works	
	This work	Theory [ref. 35]	Experiment [ref. 42]
a (Å)	4.73	4.744	4.78
B_0 (GPa)	147.63	147	148
$B_0^{'}$	4.15	4.14	—

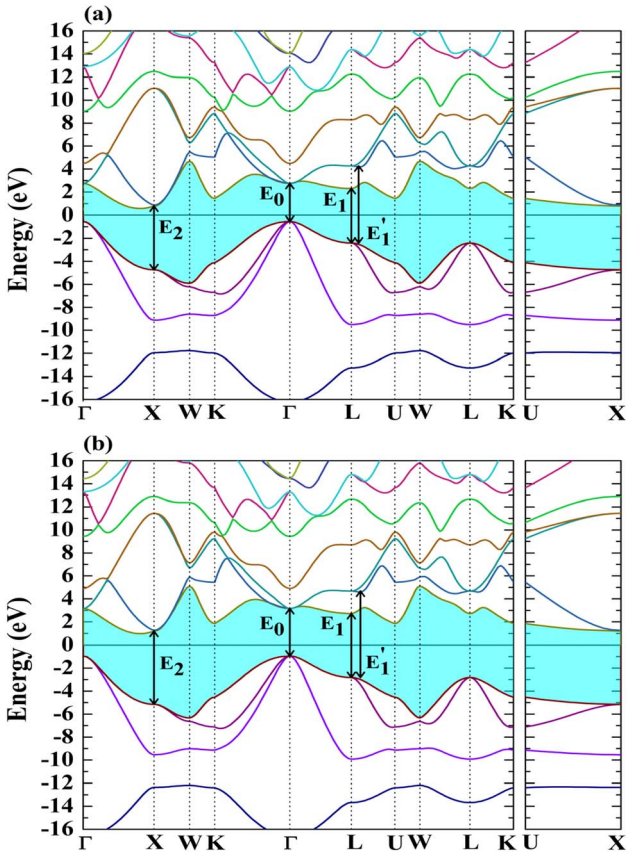

Fig. 1 Band structure of BAs calculated using (a) LDA and (b) LDA with RS.

Self-energy is one of the fundamental concepts that accounts for the difference between the theoretical eigenvalues and the experimental excitation energies. The self-energy correction of the conduction bands in several IV and III–V semiconductors is independent of energy in general. Therefore, RS of all the conduction bands to higher energies to reproduce the experimental band gap has emerged as a common practice.[101] We have also applied RS so that the band gap at Γ coincides with the experimental gap 4.12 eV.[43] This manifests as a shift in the excitation energies to 4.12 eV at Γ, 5.55 eV at L and 6.34 eV at X. Furthermore, the excitation energy $E_1^{'}$ at symmetry point L changes to 7.50 eV. These excitation energies are marked in Fig. 1(b).

It is worthy to note that the band structure of BAs partly resembles with that of Si. Essentially in Si, the heteropolar gap at the X-point is zero, subscribing to its covalent nature. In contrast, BAs has a finite heteropolar gap (~2.82 eV) that is less than the other III–V (3–4 eV range)[102] and II–VI (7–12 eV range)[102] compounds. This confirms the highly covalent nature of bonding in BAs. The ionicty,[102] on the basis of the scale $f_i = 0.91 - \frac{2}{E_h}$ proposed by Phillips, turns out to be 0.20, compared to 0.71 and 0.67 for ZnS[103] and ZnSe,[103] respectively. Interestingly, Grunert *et al.* pointed out the close relation between ionicity and the e–h interaction.[45] This is elaborated further in the forthcoming section.

4.2. Optical properties

The results for the real and imaginary parts of the dielectric function, refractive index and reflectivity from RPA, ALDA, LRC and BS were explored. In case of LRC the results deduced taking the $\alpha = 0.29$ are consistent and follow a systematic trend. Therefore, the results using $\alpha = 0.29$ are presented. However, the relative performance of other values of α on the optical properties is discussed at length separately. In all figures, the spectra with and without considering LFE are included. The results with and without considering LFE are marked as LF and NLF, respectively.

4.2.1. Dielectric functions. The dielectric function is a complex quantity. The real part (ε_1) gives the polarization induced by the field, and the imaginary part (ε_2) describes absorption.

4.2.1.1. Imaginary part of the dielectric function. The ε_2 spectra obtained while considering RPA and the three kernels with and without LFE are plotted in Fig. 2. The standard practice to link the optical absorption spectrum with band structure requires identification of peaks, as described in Fig. 1. The interband transitions are marked by vertical downward arrows and labeled E_0, E_1, E_2 and $E_1^{'}$, respectively. The absorption onset (E_0) is seen at around 4.08 eV in RPA and all three XC kernels, namely ALDA, LRC and BS. A shoulder-like structure is observed around 5.61 eV in all the spectra from the three kernels. However, in LRC, this structure is more visually appealing. One observes that, on incorporating LFE, the line shape of the spectra shifts downward in the energy region of 4 to 6 eV. The intensity of peak E_2 decreases by 16.15%, 18.70%, 2.30% and 10% in the RPA, ALDA, LRC and BS spectra, respectively. A very small blueshift in the energy position of peak E_2 is observed. Energy positions obtained from RPA, ALDA, LRC and BS are given in Table 2.

In order to see the influence of the e–h interaction, the ε_2 spectra in the selective energy region lying in the 3.5 to 4.5 eV (the onset region) and 4.5 to 6.5 eV (the region around peak E_1) ranges, are enlarged in Fig. 3. Here, comparison of the results of LRC and BS with those of the RPA and ALDA clearly reveals the influence of e–h interactions or excitonic effects. The line shapes of LRC and BS, in both regions, show a significant upward shift in intensity and redshift in energy in comparison to RPA. A similar trend is noted for the ε_2 spectra without considering LFE. As described by Azhikodan *et al.*, such features clearly signify the presence of excitonic effects.[104] These results are in good agreement with the experimental results obtained by Song *et al.* using spectroscopic ellipsometry.[43] Previously, Bushick *et al.* reported the ε_2 spectra with excitonic effects using the BSE method.[28] Barboza *et al.* reported an exciton binding energy of 133 meV for the Γ–Γ transition using the BSE method and 23.66 meV using the hydrogen-like model. Such variation is a manifestation of the large static dielectric constant of BAs and overestimates the binding energy.[38] In the LRC, this fundamental attribute is well captured by the α-parameter and hence adequately describes the excitonic behaviour. The inclusion of LFE further takes care of the interactions at work in projecting the excitonic features. In indirect band gap materials, small

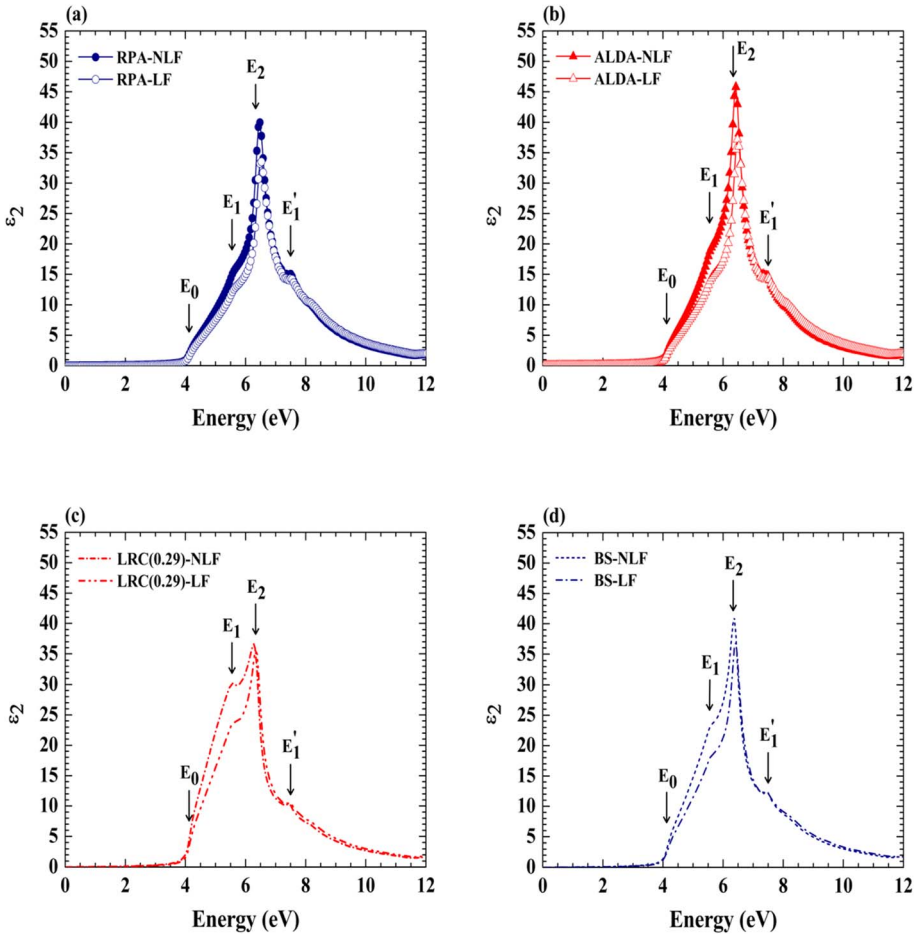

Fig. 2 Imaginary part of the dielectric function (ε_2) from (a) RPA, (b) ALDA, (c) LRC, and (d) BS.

Table 2 Energy position (in eV) of the peaks in the ε_2 spectra considering LFE. Second column shows the direct energy gap at symmetry points (SP) with RS

Peak label and SP	LDA + RS	RPA	ALDA	LRC ($\alpha = 0.29$)	BS
E_0, Γ	4.12	~4.08	~4.08	~4.08	~4.08
E_1, L	5.55	~5.61	~5.61	~5.61	~5.61
E_2, X	6.34	6.53	6.48	6.33	6.43
$E_1^{'}$, L	7.50	7.35	7.35	7.35	7.35

overlap of Bloch functions at the band extrema leads to the feeble excitonic effects on the absorption spectra. Notably, our calculations using LRC and BS kernels are in good agreement with the findings of other workers.[28,38,43]

4.2.1.2. Real part of the dielectric function. The real part of dielectric function (ε_1) derived from RPA, ALDA, LRC and BS are presented in Fig. 4. The values of the high-frequency dielectric constant (ε_∞) from RPA, ALDA, LRC and BS with and without LFE are listed in Table 3. Buckeridge and Scanlon[30] reported ε_∞ = 9.881 using QSGW + BSE, whereas Acharya *et al.*[37] reported a value of 8.75. Our calculations using LRC and BS, considering LFE, are in good agreement with these values.

One can use ε_1 to find ε_∞.[105] The static dielectric constant (ε_s) is written as:[106]

$$\varepsilon_s = \varepsilon_\infty + \varepsilon_l. \quad (15)$$

The ε_∞ is measured at frequencies well above the long-wavelength longitudinal-optic (LO) mode frequency but below the optical absorption edge. The second term on the right-hand side of eqn (15) is the lattice contribution ε_l, which arises because the LO modes in heteropolar semiconductors produce a macroscopic electric moment that separates them in energy from the transverse optical (TO) modes. The frequencies of these modes are related to the dielectric constants by the Lyddane–Sachs–Teller relation:[107,108]

$$\frac{\varepsilon_s}{\varepsilon_\infty} = \left(\frac{\omega_{LO}}{\omega_{TO}}\right)^2. \quad (16)$$

With the use of ε_∞ values given in Table 3, and taking ω_{LO} = 708.12 cm^{-1} and ω_{TO} = 702.95 cm^{-1} from ref. 28, ε_s is calculated.

Table 3 reveals that the inclusion of LFE causes a reduction in ε_∞. Also, the similar values of the two dielectric constants, ε_∞ and ε_s, lead to some important observations. Firstly, it indicates a small charge transfer between the B and As atoms. Secondly, it

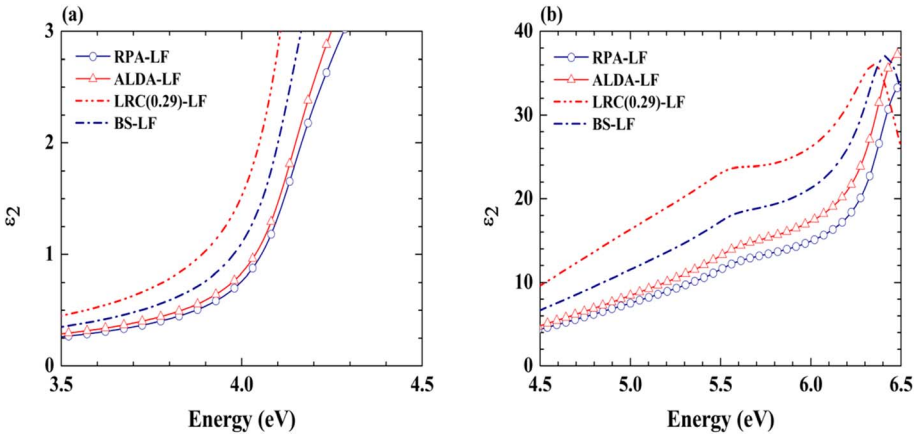

Fig. 3 Imaginary part of the dielectric function (ε_2) in the range of (a) 3.5 to 4.5 eV and (b) 4.5 to 6.5 eV.

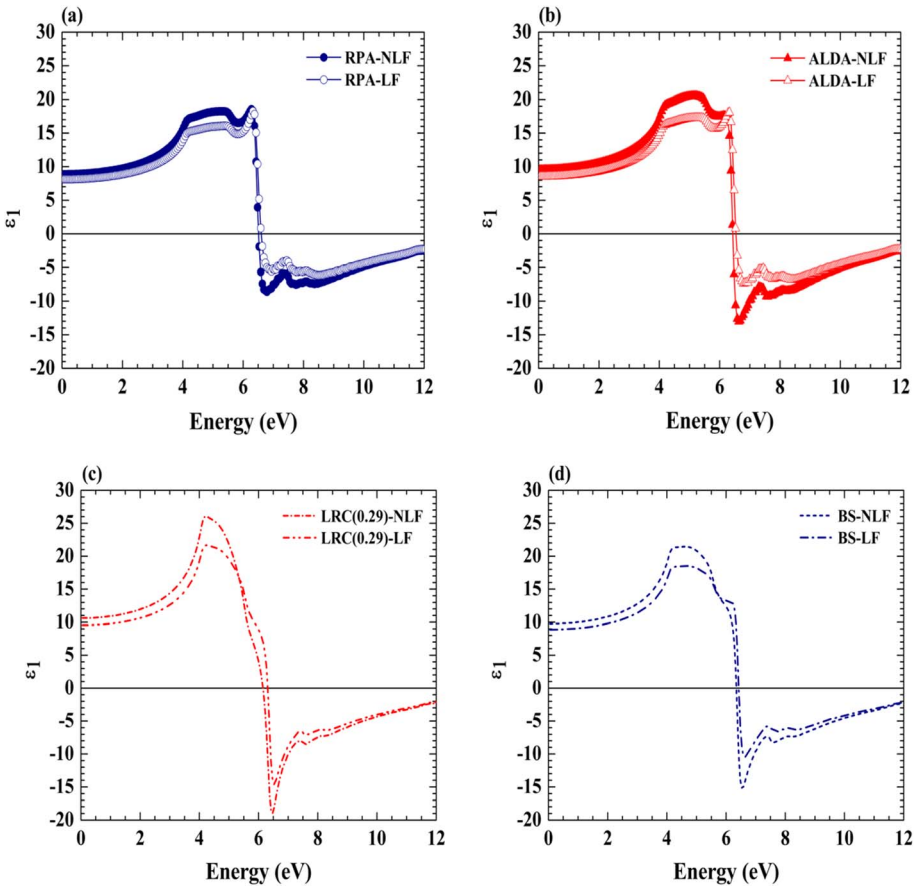

Fig. 4 Real part of the dielectric function (ε_1) from (a) RPA, (b) ALDA, (c) LRC, and (d) BS.

indicates that the scattering of electrons by polar optical phonons is weaker than that in other III–V semiconductors, which possibly leads to relatively high electron and hole mobilities.[28,109] Thirdly, the lattice contribution ε_l after incorporating LFE, obtained using eqn (15) is 0.12, 0.13, 0.14 and 0.13 for RPA, ALDA, LRC and BS, respectively. These low values signify the high degree of covalency in the BAs.

Using the hydrogenic model, one can calculate the exciton binding energy $E_b = 13.6\ \text{eV}\ \mu^*/{\varepsilon_\infty}^2$.[28] The LRC and BS kernels deliver E_b values of 38 and 44 meV, respectively. These are very close to the GW–BSE data reported by Bushick *et al.* (*i.e.*, 43 meV).[28] Such magnitudes of E_b indicate that the excitons are relatively stable in BAs and do not thermally dissociate at room temperature. This exciton binding energy is larger than that of GaAs (~6.44 meV), which is widely used in optoelectronics.

Table 3 Comparison of the ε_∞ and ε_s of BAs

		RPA	ALDA	LRC ($\alpha = 0.29$)	BS	Other
ε_∞	NLF	8.87	9.53	10.62	9.77	9.881 [ref. 30]
	LF	8.14	8.52	9.55	8.87	8.75 [ref. 37]
ε_s	NLF	9.00	9.67	10.78	9.91	
	LF	8.26	8.65	9.69	9.00	

This, together with the lower recombination rate reported in thermoelectric properties, indicates that BAs is an excellent choice for photovoltaic devices.[6]

4.2.2. Refractive index. In Fig. 5, the real part of the refractive index ('n') evaluated from various XC kernels is plotted. In the limit $E \to 0$, the real part of the refractive index ('n') gives a vital quantity:[110]

$$n|_{E\to 0\ \mathrm{eV}} = \sqrt{\varepsilon_\infty} \tag{17}$$

The curves of Fig. 5 verify this relationship. The value of $n|_{E\to 0\mathrm{eV}}$, considering LFE, is 2.85, 2.92, 3.09 and 2.98 for RPA, ALDA, LRC and BS, respectively. Kang *et al.* measured the optical refractive index by Fabry–Pérot interferometer and reported the refractive index to be in the $n = 3.29$ to 3.04 range.[42] Song *et al.* found $n = 3.04 \pm 0.02$ using both spectroscopic ellipsometry and transmission and reflection spectroscopy.[43] Mahat *et al.* measured $n = 3.02 \pm 0.06$ at 778 nm using Brewster angle measurements.[44] Our results from LRC and BS are in good agreement with all these results.

In the region 4 to 7 eV, the trends of the line shapes from RPA and ALDA are similar. In the region of 4 to 6 eV, 'n' changes linearly with energy, followed by a small dip in the RPA and ALDA spectra. A clear maximum in the RPA-NLF(LF) and ALDA-NLF(LF) can be seen at 6.38(6.38) and 6.33(6.38) eV, respectively. For both RPA and ALDA, inclusion of LFE causes a decrease in the intensity of this peak. In contrast, a broad structure in the energy region of 4 to 5.5 eV, followed by a less intense peak structure, is observed in the LRC and BS spectra. On including LFE, this broad structure shifts downwards. Overall, in the 4 to 7 eV region, the visual appearance of the RPA and ALDA spectra differs from those of BS and LRC. These differences are due to excitonic effects captured by LRC and BS kernels. A similar type of behavior is also noted in calculations with and without excitonic effects, as reported by Song *et al.*[43] Beyond 7 eV, the line shape shifts upwards slightly after including LFE for RPA and all three XC kernels; however, the differences are very small.

Fig. 6 shows the imaginary part of the refractive index 'k'. The vertical arrows indicate the positions of several interband transitions labeled according to direct gap energies at SP [see Fig. 1(b)]; the energetic positions are given in Table 4. A shoulder-like structure is observed in the RPA and all three XC

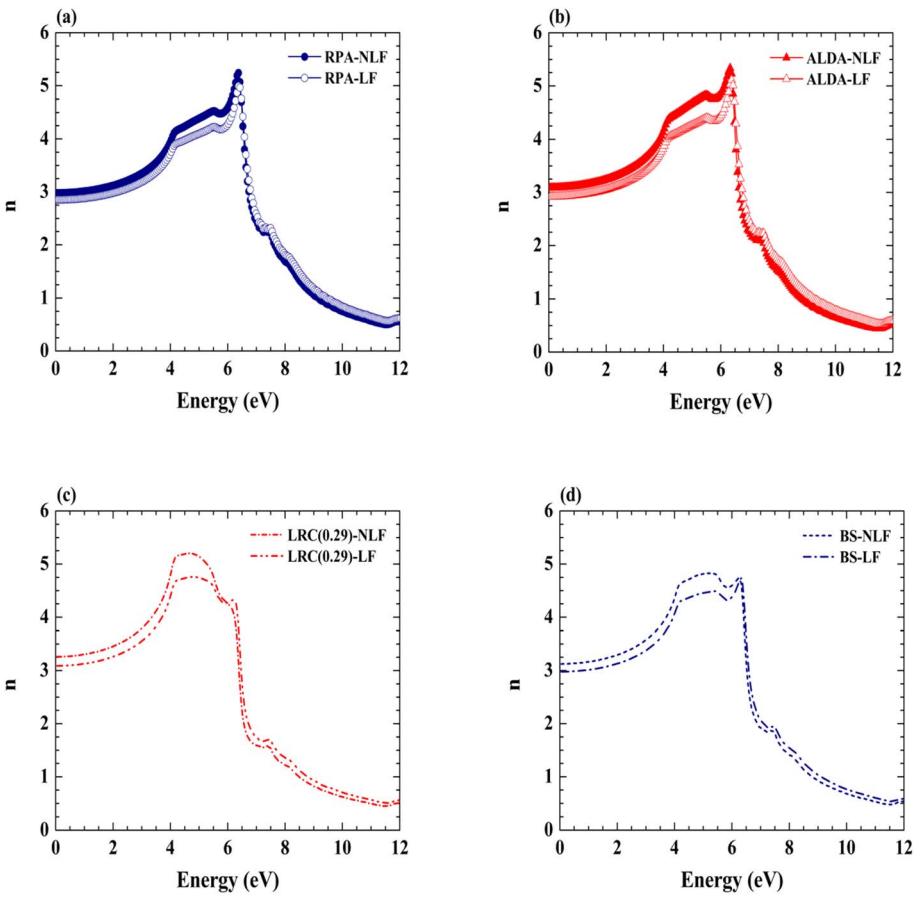

Fig. 5 Real part 'n' of the refractive index using (a) RPA, (b) ALDA, (c) LRC, and (d) BS.

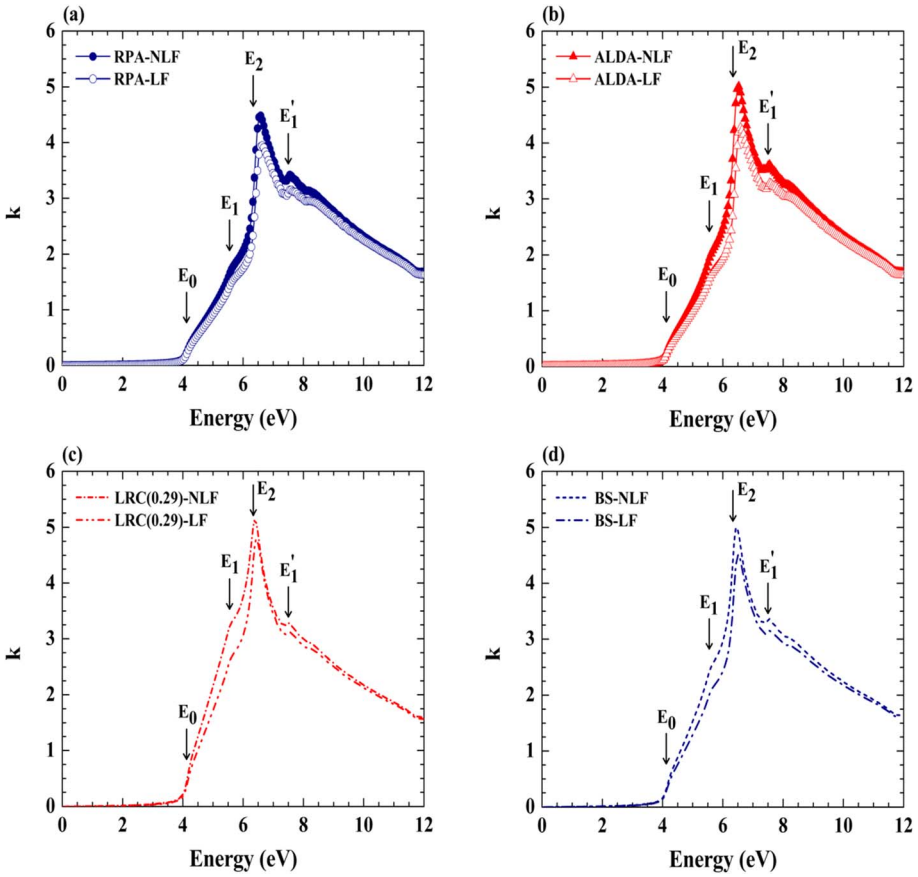

Fig. 6 Imaginary part '*k*' of the refractive index using (a) RPA, (b) ALDA, (c) LRC, and (d) BS.

Table 4 Energy position (in eV) of the peaks in the '*k*' spectra considering LFE. Second column shows the direct energy gap at SP with RS

Peak label and SP	LDA + RS	RPA	ALDA	LRC ($\alpha = 0.29$)	BS
E_0, Γ	4.12	~4.08	~4.08	~4.08	~4.08
E_1, L	5.55	~5.61	~5.61	~5.61	~5.66
E_2, X	6.34	6.63	6.58	6.43	6.53
$E_1^{'}$, L	7.50	7.55	7.55	7.55	7.55

kernel spectra around peak E_1. After considering LFE, the line shape around this peak shifts downward in all approximations. However, the line shapes of LRC and BS kernels shift upward slightly with respect to those of RPA and ALDA. This may be a signature of the continuum excitonic effect projected by the LRC and BS kernels. Moreover, the inclusion of LFE causes a negligible blueshift in the energy positions of peak E_2 for RPA and all three XC kernels. However, the intensity of peak E_2 reduces by 12.00%, 14.79%, 6.83% and 9.61% for RPA, ALDA, LRC and BS, respectively. The shapes of the curves of '*k*' using LRC and BS are in reasonable agreement with the results reported by Song *et al.*[43]

4.2.3. Reflectivity. The reflectivity spectra obtained using RPA and the three XC kernels are shown in Fig. 7; energy positions are given in Table 5. The vertical downward arrows indicate the positions of several interband transitions marked in Fig. 1(b). For the sake of discussion, the calculated reflectivity spectra are divided into three regions.

The first region (0–8 eV) marks interband transitions, and the second region (8–12 eV) shows a plateau-like trend. It is noted that the peaks labeled E_0 and E_1 in all the calculated spectra appear as a shoulder around 4.13 and 5.56 eV, respectively. On considering LFE, all the calculated spectra show downward shifts, and the most intense peak E_2 shows a very small blueshift of 0.05 eV for RPA, ALDA and BS. As shown in the inset of Fig. 7, beyond 12 eV, a gradual decrease in reflectivity spectra is observed. This may be related to transmission onset because, as prescribed by Mendlowitz, when ε_1 is negative, the material is reflecting, and when ε_1 is positive, the material is transmitting.[111] This decrease in reflectivity is also related to the plasmon peak in the EELS spectra as discussed in the next section.[112]

4.3. Electron energy loss spectra

The function representing characteristic energy losses or plasmon oscillations is one of the most important among those suitable for the description of microscopic and macroscopic properties of a solid. The EELS obtained using the four models are presented in Fig. 8. To analyze the effect of the local field on EELS, we also plotted the results obtained without considering LFE.

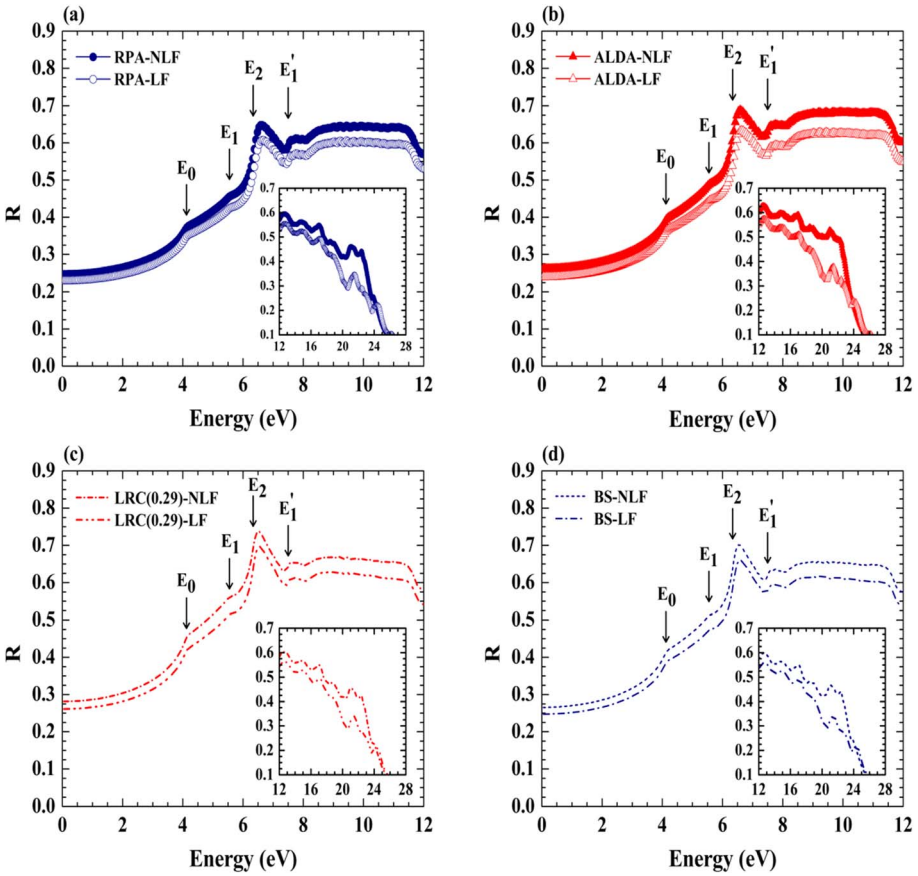

Fig. 7 Reflectivity spectra using (a) RPA, (b) ALDA, (c) LRC, and (d) BS. Insets show enlarged view of the spectra in the 12–28 eV range.

Table 5 Energy position (in eV) of the peaks in the R spectra considering LFE. Second column shows the direct energy gap at SP with RS

Peak label and SP	LDA + RS	RPA	ALDA	LRC ($\alpha = 0.29$)	BS
E_0, Γ	4.12	~4.13	~4.13	~4.13	~4.13
E_1, L	5.55	~5.56	~5.56	~5.56	~5.61
E_2, X	6.34	6.68	6.63	6.53	6.58
$E_1^{'}$, L	7.50	7.76	7.76	7.76	7.76

By comparing the EELS with the optical spectra, particularly ε_1 and ε_2, the type of excitation responsible for the various peaks can be determined. In general, such peaks can be associated with interband transitions or plasmon excitation. If ε_2 is large at an energy of loss spectra. This feature is attributed to single particle interband excitation. In addition, features located at energy losses where ε_1 passes through zero (going from negative to positive) signify collective excitations known as plasmons.[113–115] For the sake of discussion, we divide EELS into three regions. The first region (0–21 eV) includes peaks A, B and C, the second region (21–24 eV) includes peaks D, E and F, and the third region includes peak G. The energy positions of all these peaks are given in Table 6.

Visually, the EEL spectra obtained using all the approximations are similar. The reason may be the reduced relevance of the $1/|\boldsymbol{q}|^2$ dependence for EELS. However, this feature, which is well captured by LRC and BS kernels, is more important for the absorption spectra to capture the e–h interaction.[116] Moreover, the spectra from LRC and BS kernels contain excitonic effects, but, since they are screened, they are less visible than in the absorption spectrum. Instead, the EEL spectrum is dominated by plasmons.

First, we focus on the effect of the local field on EELS. Peaks in EELS with LFE are indicated by vertical downward arrows. In the first region, after incorporating LFE, it is observed that the intensities of the peaks A and B are almost the same. Peak C becomes a visually clear peak. In the second region, without considering LFE, it is noted that D is a shoulder, E is the peak with maximum intensity, and F is a less intense peak. On including LFE, the shoulder-like structure D emerges clearly. Furthermore, the intensities of peaks E and F become almost equal in all the approximations. In the third region, we observe that the intensity of peak G increases slightly on incorporating LFE.

Second, we discuss the origin of various peaks in EELS. In the first region, the energy positions of peaks A, B, and C obtained from RPA, ALDA, LRC and BS are almost the same. Hence, it is appropriate to refer to the average value of these energy positions. We noted a much less intense peak in EELS-NLF(LF) around 5.82(5.87) eV (peak A) in all our calculations.

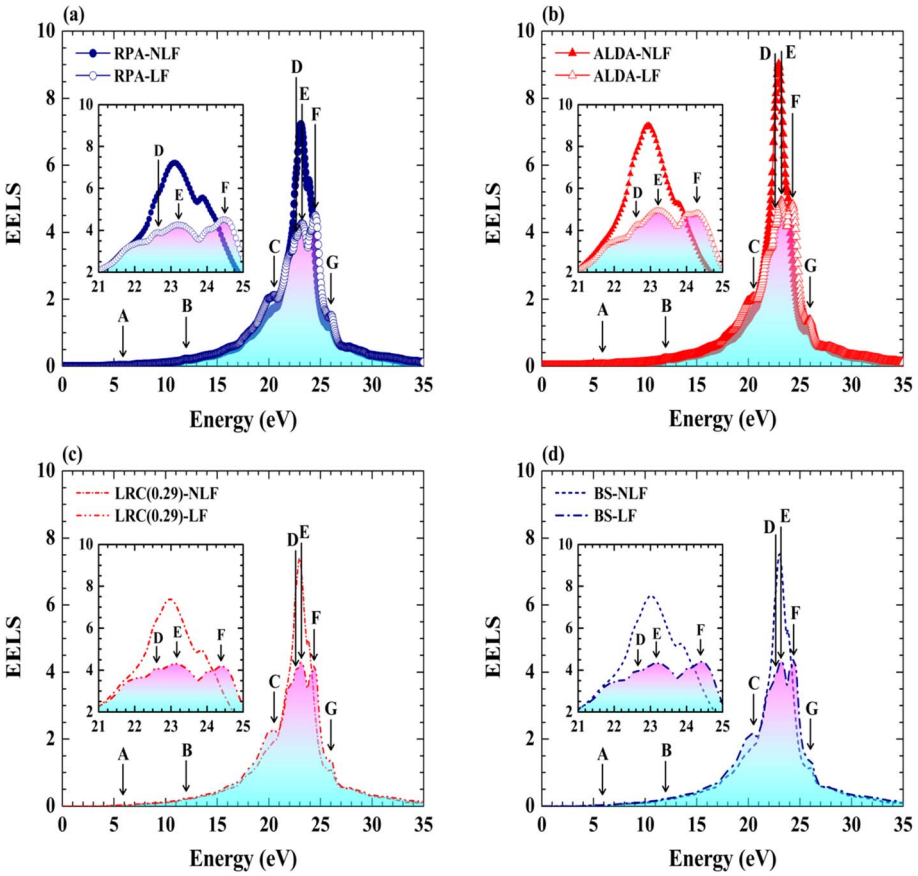

Fig. 8 EELS using (a) RPA, (b) ALDA, (c) LRC, and (d) BS. Insets show enlarged view of the spectra in the 21–25 eV range.

From the ε_2 spectra discussed in the earlier section, it can be interpreted that this peak is due to interband transitions. Peak B appears around 11.99 eV in the EELS from all the approximations. This peak may originate from an electronic transition from the second band below the Fermi level to the third band above the Fermi level. Furthermore, peak C, located around 20.51 eV in EELS, may originate from the transition from the fourth valence band below the Fermi level to the fourth conduction band above the Fermi level.

Generally, the most prominent peak in the EELS is identified as the plasmon peak, which corresponds to the excitation of longitudinal oscillations.[117] Plasma resonances have a simple relationship to the dispersive part of the dielectric function. A vanishing ε_1 (or crossing the $\varepsilon_1 = 0$ axis with a positive slope) is a necessary condition for the occurrence of plasma oscillations, but it is not sufficient. In addition, the amplitude of the ε_2 spectra should also be small.[118] Such a situation can be examined by the curves plotted in Fig. 9.

In the 5 to 8 eV region of the ε_1 curve, we observe that ε_1 crosses the zero axis (*i.e.* $\varepsilon_1 = 0$) from positive to negative at values of around 6.48(6.58), 6.43(6.53), 6.12(6.28) and 6.33(6.38) eV for RPA-NLF(LF), ALDA-NLF(LF), LRC-NLF(LF) and BS-NLF(LF), respectively. Interestingly, in the region of 5 to 8 eV in the ε_2 curve, the ε_2 amplitude is quite high, and it is dominated by interband transitions. Therefore, the EELS do not

Table 6 Energy position (in eV) of peaks in EELS with and without LFE. Peaks C and D in EELS-NLF are shoulder-like structures

	Without LFE (NLF)				With LFE (LF)			
Peak label	RPA	ALDA	LRC	BS	RPA	ALDA	LRC	BS
A	5.82	5.82	5.82	5.82	5.87	5.87	5.87	5.87
B	11.99	11.94	11.99	11.99	11.99	11.99	11.99	11.99
C	~20.51	~20.36	~20.51	~20.41	20.51	20.51	20.51	20.51
D	~22.60	~22.60	~22.60	~22.60	22.65	22.65	22.60	22.65
E	23.11	22.96	22.96	23.01	23.21	23.21	23.16	23.16
F	23.88	~23.78	23.83	23.83	24.49	24.29	24.39	24.39
G	25.97	25.92	25.97	25.97	26.02	25.97	26.02	26.02

satisfy the condition for the occurrence of the plasmon peak; hence, no plasmon peak occurs in this region.

In the 21 to 24 eV region, we observed that ε_1 crosses the zero axis from negative to positive value around 22.96(22.60), 22.86(22.91), 22.81(22.50) and 22.91(22.60) eV for RPA-NLF(LF), ALDA-NLF(LF), LRC-NLF(LF) and BS-NLF(LF), respectively. At such high energies, the amplitudes of the ε_2 values are quite low. As discussed earlier, we found a clear maximum intensity peak in EELS without considering LFE at 23.11, 22.96, 22.96 and 23.01 for RPA, ALDA, LRC and BS, respectively. Instead, after incorporating LFE, a clear two-peak structure at energies between 23 and 25 eV and separated by ~1.2 eV is noted for all the approximations. However, after including LFE, peak E in the EELS-LFE, observed at 23.21, 23.21, 23.16 and 23.16 for RPA, ALDA, LRC and BS, respectively, better correlates with the zero crossing in ε_1, reasonably satisfying the necessary and sufficient conditions for the occurrence of plasma oscillation in this region. It is worth noting that the F peak does not satisfy the criterion of plasmon effects, as per the description by Dash *et al.*,[78] which may originate from collective excitations. Due to the lack of experimental results for EELS of the BAs, discussions on the plasmon peak are ongoing and are a subject of further investigation. However, it may be noted that the range lie ~3.30–3.93 eV for $\Delta E_{1/2}$ in the E peak, is nearly of the order of 3.20 eV observed for corresponding peak in Si.[113]

For more clarity, the calculated values of ε_1 and ε_2 in the vicinity of the prominent peak in EELS are highlighted in Fig. 9. The figure reveals the effect of the local field on the zero crossing of the ε_1 curve, and it can be noted that the zero crossing of ε_1 shows a redshift for RPA, LRC and BS, whereas a blueshift is seen for ALDA.

4.4. Effect of parameter α on the optical properties and electron energy loss spectra

As discussed in the earlier section, three values of α, *viz.* 0.29, 0.41, and 0.71, are considered. These are determined by the formula proposed by Botti *et al.*,[73] linear interpolation of α values obtained using symmetric and antisymmetric FFs of AlAs, GaAs, InAs, and lastly using symmetric and antisymmetric FFs of BAs, as reported by Da Ng and Danner,[100] respectively. The objective of this section is to justify the reason for selecting the value 0.29 among the three alternatives. The optical and EEL spectra shown by $\alpha = 0.29$ (ionicity = 0.20) and 0.41 are similar, while the spectra with $\alpha = 0.71$ (ionicity = 0.24), show some deviations. A close look at the FF reveals that Da Ng and Danner used local pseudopotential FFs.[100] In covalent compounds, one

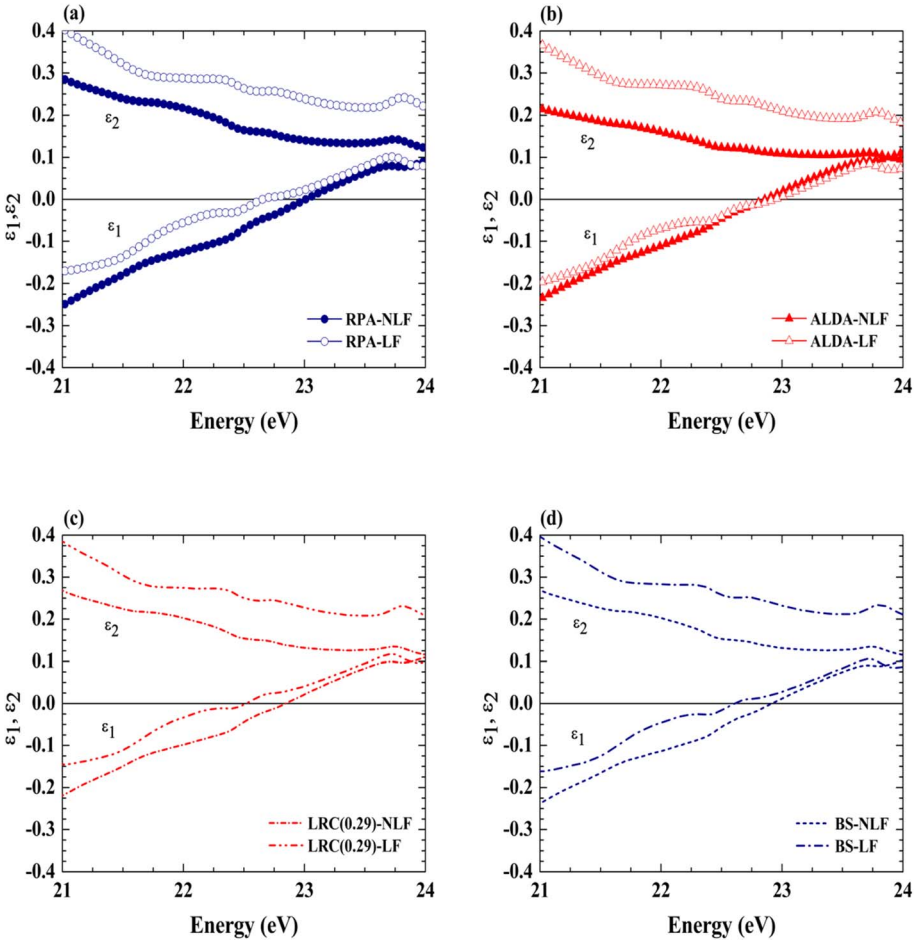

Fig. 9 Real (ε_1) and imaginary (ε_2) parts of the dielectric function in the plasmon energy region using (a) RPA, (b) ALDA, (c) LRC, and (d) BS.

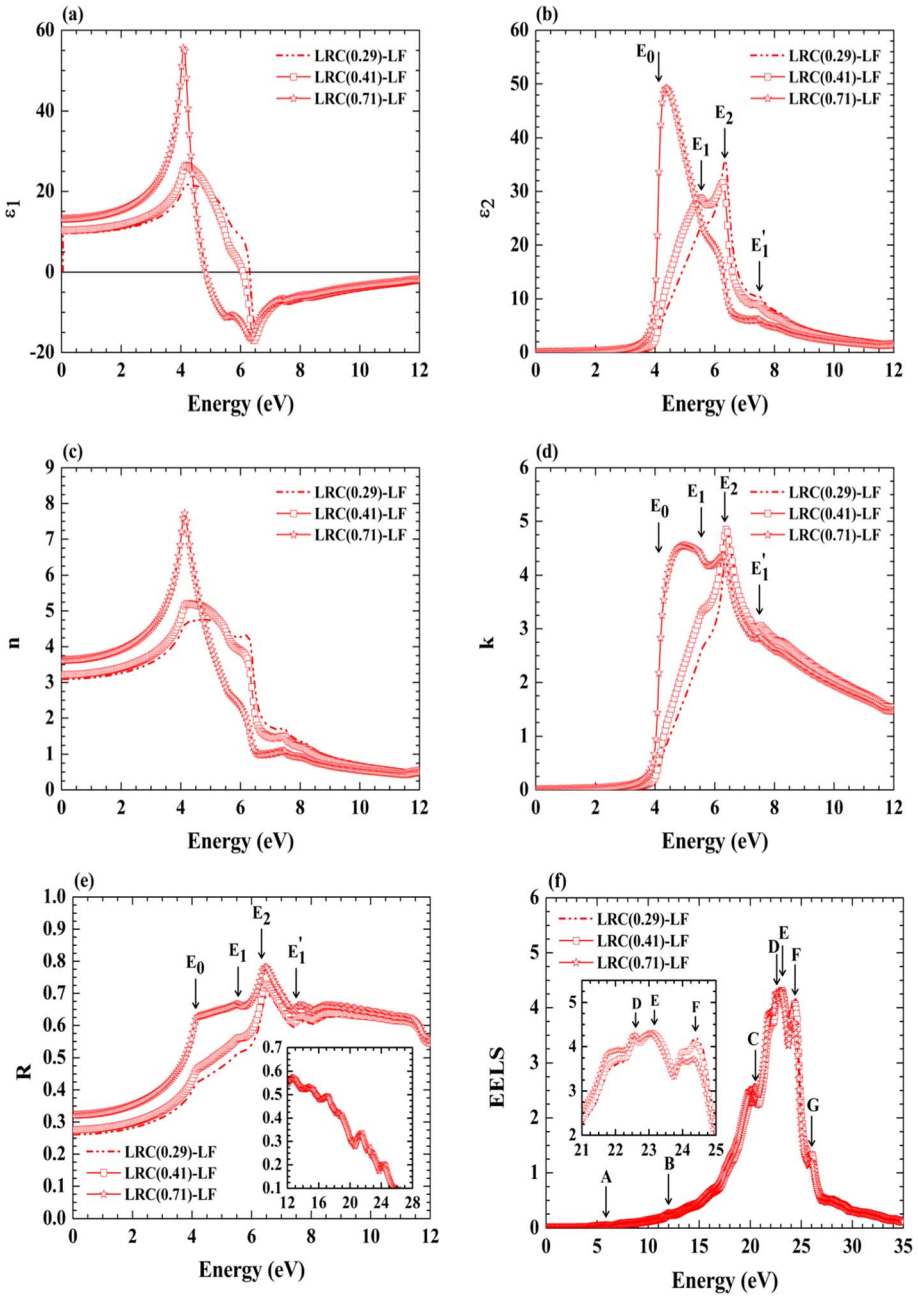

Fig. 10 Optical and EEL spectra of BAs using LRC-LF with three different choices of α. Insets in (e) and (f) show enlarged views of the spectra.

Table 7 Energy position (in eV) of the peaks in the ε_2 of BAs computed using LRC-LF with three different values of α

Peak labels	LRC ($\alpha = 0.29$)	LRC ($\alpha = 0.41$)	LRC ($\alpha = 0.71$)
E_0	~4.08	~4.08	~3.98
E_1	~5.61	5.51	4.39
E_2	6.33	6.28	~6.12
$E_1^{'}$	7.35	7.35	7.35

needs to consider the *l*-dependent pseudopotential FFs. Thus, inadequate treatment of the non-local effects leads to less effective treatment of the bonding nature. This may be the reason for the modest results with $\alpha = 0.71$. Indeed, however, the LRC is highly sensitive to the choice of α. All parts of Fig. 10 exhibit the effect of parameter α on various optical properties.

Table 8 Energy position (in eV) of the peaks in the '*k*' of BAs computed using LRC-LF with three different values of α

Peak labels	LRC ($\alpha = 0.29$)	LRC ($\alpha = 0.41$)	LRC ($\alpha = 0.71$)
E_0	~4.08	~4.08	~3.98
E_1	~5.61	5.56	5.00
E_2	6.43	6.38	6.28
$E_1^{'}$	7.55	7.55	7.50

Table 9 Energy position (in eV) of the peaks in the R of BAs computed using LRC-LF with three different values of α

Peak labels	LRC ($\alpha = 0.29$)	LRC ($\alpha = 0.41$)	LRC ($\alpha = 0.71$)
E_0	~4.13	~4.13	~4.18
E_1	~5.56	~5.51	5.51
E_2	6.53	6.53	6.48
$E_1^{'}$	7.76	7.76	7.60

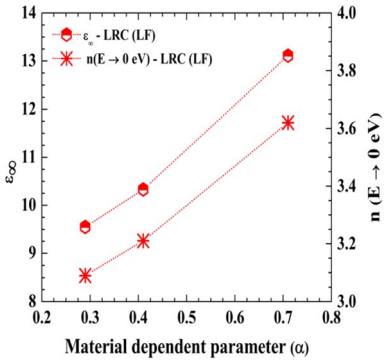

Fig. 11 Variations in ε_∞ and 'n' with parameter α for LRC-LF.

Fig. 10(b) and (d) reveal that with the increase in α, the intensity of the shoulder E_1 increases and is converted into a well-observed peak at $\alpha = 0.71$. In the spectra with $\alpha = 0.71$, a significant redshift in the energy of peak E_1 is noted compared to that with $\alpha = 0.29$. Furthermore, one can observe that the impact of a higher value of α is more apparent on peak E_1 than on peaks E_2 and $E_1^{'}$. This points out sensitivity of excitonic feature on α. One observes from Fig. 10(a) and (c) that the values of ε_∞ and 'n' in low energy limit increase with the increase in α. Fig. 10(d) and (e), further reveal that with increasing values of α, the line shape of 'k' and R differ by ~6 eV and do not change after ~9 eV. Fig. 10(f) shows EELS for different values of α. It is visually clear that the shapes of the EELS are almost the same with increasing values of α. However, as shown in the inset of Fig. 10(f), there is a feeble decrease in the intensity of peak F with increasing α. Tables 7–9 summarize the peak positions in ε_2, 'k', and R.

The variation of ε_∞ and 'n' in the low-energy limit with parameter α are plotted in Fig. 11. One notices a similar trend with and without considering LFE. This reveals that the agreement between LRC and the experimental curve worsens with an increasing value of α.

5. Conclusions

Ground state calculations of BAs were performed by applying the FP-LAPW method. The calculation simulates the ground state, giving structural parameters well in accordance with the experimental results. The material is found to be a semiconductor with an indirect band gap of 1.11 eV and a direct band gap of 3.30 eV. The SC of 0.82 eV is applied in all linear response calculations to explore the optical and EEL spectra. The calculated spectra of ε_1, ε_2, n and k from LRC and BS considering LFE are in good agreement with the earlier experimental studies. The comparison reveals the importance of the inclusion of e–h interaction and LFE in the calculations. The LRC calculations of optical spectra confirm the inadequacy of earlier calculations in dealing with dielectric screening, which is more appropriately captured by the LRC. A clear impact of LFE on the optical spectra is noted; however, the impact is not as intense as observed in other II–VI and III–V compound semiconductors. This observation is in line with the fact that LFE increases with increasing ionicity, whereas BAs is covalent.

The EELS obtained using all the approximations show similar trends. Of the three values of α, *viz.* 0.29, 0.41 and 0.71, used in the current LRC calculations, the value $\alpha = 0.29$, obtained using the scheme of Botti *et al.*,[73] shows good agreement of the optical properties with the results from the BS kernel. The spectra using $\alpha = 0.41$ are also in good agreement with the BS kernel. The hydrogenic model gave the binding energies of excitons $E_b = 38$ and 44 meV, in good agreement with the GW–BSE data (43 meV). The deviations shown by the spectra with $\alpha = 0.71$ are due to the less effective FFs reported by Da Ng and Danner[100] because these are devoid of l-dependent effects. Therefore, in summary, the scheme proposed by us to find the α parameter using symmetric and antisymmetric FFs also works well for BAs. The current results show that the inclusion of the e–h interaction and LFE plays a significant role in ascertaining the optical properties of BAs, which may lead to potential applications in optoelectronics.

The fact that the semiconductors are the next generation materials essentially for micro and optoelectronics devices. BAs can withstand a high range of temperatures. The theoretical results obtained in this work can be useful for optoelectronic and photovoltaic applications of BAs. To unleash the full potential of the technological applications of semiconductors, LRC can be applied by finding α using the scheme proposed in this work.

Author contributions

Nikhil Joshi: data curation (equal), formal analysis (lead), investigation (lead), methodology (lead), software (equal), validation (equal), visualization (equal), writing/original draft preparation (lead). Shruti Jangir: data curation (equal), software (equal), validation (equal), visualization (equal), funding acquisition (equal), writing/review & editing (equal). K. B. Joshi: conceptualization (lead), funding acquisition (equal), project administration (lead), resources (lead), supervision (lead), writing/review & editing (equal).

Conflicts of interest

The authors have no conflicts to disclose.

Data availability

The data that support the findings of this study are available from the corresponding author upon reasonable request.

Acknowledgements

This work is partially supported by the RUSA 1.0 program of the MHRD, New Delhi. One of the authors (SJ) is grateful to the UGC, New Delhi, for awarding the JRF.

References

1 L. Lindsay, D. A. Broido and T. L. Reinecke, *Phys. Rev. Lett.*, 2013, **111**, 025901, DOI: 10.1103/PhysRevLett.111.025901.
2 T. Feng, L. Lindsay and X. Ruan, *Phys. Rev. B*, 2017, **96**, 161201(R), DOI: 10.1103/PhysRevB.96.161201.
3 S. Li, Q. Zheng, Y. Lv, X. Liu, X. Wang, P. Y. Huang, D. G. Cahill and B. Lv, *Science*, 2018, **361**, 579, DOI: 10.1126/science.aat8982.
4 J. S. Kang, M. Li, H. Wu, H. Nguyen and Y. Hu, *Science*, 2018, **361**, 575, DOI: 10.1126/science.aat5522.
5 F. Tian, B. Song, X. Chen, N. K. Ravichandran, Y. Lv, K. Chen, S. Sullivan, J. Kim, Y. Zhou, T.-H. Liu, *et al.*, *Science*, 2018, **361**, 582, DOI: 10.1126/science.aat7932.
6 I. Amghar, M. Ziati, A. Boubekraoui and H. Ez-Zahraouy, *Phys. Scr.*, 2025, **100**, 0159a7, DOI: 10.1088/1402-4896/ada06d.
7 D. J. Stukel, *Phys. Rev. B*, 1970, **1**, 3458, DOI: 10.1103/PhysRevB.1.3458.
8 R. M. Wentzcovitch and M. L. Cohen, *J. Phys. C: Solid State Phys.*, 1986, **19**, 6791, DOI: 10.1088/0022-3719/19/34/016.
9 R. M. Wentzcovitch, M. L. Cohen and P. K. Lam, *Phys. Rev. B: Condens. Matter Mater. Phys.*, 1987, **36**, 6058, DOI: 10.1103/PhysRevB.36.6058.
10 C. Prasad and M. Sahay, *Phys. Status Solidi B*, 1989, **154**, 201, DOI: 10.1002/pssb.2221540118.
11 T. Pletl, P. Pavone, U. Engel and D. Strauch, *Physica B: Condens. Matter.*, 1999, **263–264**, 392, DOI: 10.1016/S0921-4526(98)01240-X.
12 B. Bouhafs, H. Aourag, M. Ferhat and M. Certier, *J. Phys.: Condens. Matter*, 1999, **11**, 5781, DOI: 10.1088/0953-8984/11/30/309.
13 B. Bouhafs, H. Aourag and M. Certier, *J. Phys.: Condens. Matter*, 2000, **12**, 5655, DOI: 10.1088/0953-8984/12/26/312.
14 G. L. W. Hart and A. Zunger, *Phys. Rev. B: Condens. Matter Mater. Phys.*, 2000, **62**, 13522, DOI: 10.1103/PhysRevB.62.13522.
15 H. Meradji, S. Drablia, S. Ghemid, H. Belkhir, B. Bouhafs and A. Tadjer, *Phys. Status Solidi B*, 2004, **241**, 2881, DOI: 10.1002/pssb.200302064.
16 N. Chimot, J. Even, H. Folliot and S. Loualiche, *Phys. B*, 2005, **364**, 263, DOI: 10.1016/j.physb.2005.04.022.
17 A. Zaoui, S. Kacimi, A. Yakoubi, B. Abbar and B. Bouhafs, *Phys. B*, 2005, **367**, 195, DOI: 10.1016/j.physb.2005.06.018.
18 S. Cui, W. Feng, H. Hu, Z. Feng and Y. Wang, *Comput. Mater. Sci.*, 2009, **44**, 1386, DOI: 10.1016/j.commatsci.2008.09.009.
19 R. Mohammad and Ş. Katırcıoğlu, *J. Alloys Compd.*, 2009, **485**, 687, DOI: 10.1016/j.jallcom.2009.06.042.
20 A. Boudjemline, M. M. Islam, L. Louail and B. Diawara, *Phys. B*, 2011, **406**, 4272, DOI: 10.1016/j.physb.2011.08.043.
21 M. Guemou, B. Bouhafs, A. Abdiche, R. Khenata, Y. A. Douri and S. B. Omran, *Phys. B*, 2012, **407**, 1292, DOI: 10.1016/j.physb.2012.01.132.
22 N. N. Anua, R. Ahmed, A. Shaari, M. A. Saeed, B. Ul Haq and S. Goumri-Said, *Semicond. Sci. Technol.*, 2013, **28**, 105015, DOI: 10.1088/0268-1242/28/10/105015.
23 D. A. Broido, L. Lindsay and T. L. Reinecke, *Phys. Rev. B: Condens. Matter Mater. Phys.*, 2013, **88**, 214303, DOI: 10.1103/PhysRevB.88.214303.
24 M. Guemou, A. Abdiche, R. Riane and R. Khenata, *Phys. B*, 2014, **436**, 33, DOI: 10.1016/j.physb.2013.11.030.
25 V. G. Hadjiev, M. N. Iliev, B. Lv, Z. F. Ren and C. W. Chu, *Phys. Rev. B: Condens. Matter Mater. Phys.*, 2014, **89**, 024308, DOI: 10.1103/PhysRevB.89.024308.
26 N. H. Protik, J. Carrete, N. A. Katcho, N. Mingo and D. Broido, *Phys. Rev. B*, 2016, **94**, 045207, DOI: 10.1103/PhysRevB.94.045207.
27 I. H. Nwigboji, Y. Malozovsky, L. Franklin and D. Bagayoko, *J. Appl. Phys.*, 2016, **120**, 145701, DOI: 10.1063/1.4964421.
28 K. Bushick, K. Mengle, N. Sanders and E. Kioupakis, *Appl. Phys. Lett.*, 2019, **114**, 022101, DOI: 10.1063/1.5062845.
29 A. Rastogi, P. Rajpoot and U. P. Verma, *Bull. Mater. Sci.*, 2019, **42**, 112, DOI: 10.1007/s12034-019-1758-8.
30 J. Buckeridge and D. O. Scanlon, *Phys. Rev. Mater.*, 2019, **3**, 051601(R), DOI: 10.1103/PhysRevMaterials.3.051601.
31 I. Bravić and B. Monserrat, *Phys. Rev. Mater.*, 2019, **3**, 065402, DOI: 10.1103/PhysRevMaterials.3.065402.
32 X. Chen, C. Li, F. Tian, G. A. Gamage, S. Sullivan, J. Zhou, D. Broido, Z. Ren and L. Shi, *Phys. Rev. Appl.*, 2019, **11**, 064070, DOI: 10.1103/PhysRevApplied.11.064070.
33 Y. Ge, W. Wan, X. Guo and Y. Liu, *Opt. Express*, 2020, **28**, 238, DOI: 10.1364/OE.378374.
34 W. Sukkabot, *Philos. Mag.*, 2020, **100**, 1903, DOI: 10.1080/14786435.2020.1746849.
35 K. Yaddanapudi, *Comput. Mater. Sci.*, 2020, **184**, 109887, DOI: 10.1016/j.commatsci.2020.109887.
36 X. Yang, T. Feng, J. S. Kang, Y. Hu, J. Li and X. Ruan, *Phys. Rev. B*, 2020, **101**, 161202(R), DOI: 10.1103/PhysRevB.101.161202.
37 S. Acharya, D. Pashov, M. I. Katsnelson and M. van Schilfgaarde, *Phys. Status Solidi RRL*, 2024, **18**, 2300156, DOI: 10.1002/pssr.202300156.
38 E. d. S. Barboza, A. C. Dias, L. Craco, S. S. Carara, D. R. da Costa and T. A. S. Pereira, *ACS Omega*, 2024, **9**, 47710, DOI: 10.1021/acsomega.4c07598.
39 R. Islam, S. Islam, R. H. Mojumder, Z. Khan, H. Molla, A. S. M. J. Islam and J. Park, *Mater. Today Commun.*, 2022, **33**, 104227, DOI: 10.1016/j.mtcomm.2022.104227.
40 S. Behzad and R. Chegel, *Sci. Rep.*, 2023, **13**, 21339, DOI: 10.1038/s41598-023-48654-9.
41 R. Chegel, *Sci. Rep.*, 2025, **15**, 16227, DOI: 10.1038/s41598-025-99320-1.
42 J. S. Kang, M. Li, H. Wu, H. Nguyen and Y. Hu, *Appl. Phys. Lett.*, 2019, **115**, 122103, DOI: 10.1063/1.5116025.
43 B. Song, K. Chen, K. Bushick, K. A. Mengle, F. Tian, G. A. G. U. Gamage, Z. Ren, E. Kioupakis and G. Chen, *Appl. Phys. Lett.*, 2020, **116**, 141903, DOI: 10.1063/5.0004666.

44 S. Mahat, S. Li, H. Wu, P. Koirala, B. Lv and D. G. Cahill, *Phys. Rev. Mater.*, 2021, **5**, 033606, DOI: 10.1103/PhysRevMaterials.5.033606.
45 M. Grunert, M. Großmann and E. Runge, *Phys. Rev. B*, 2024, **110**, 075204, DOI: 10.1103/PhysRevB.110.075204.
46 F. Aryasetiawan and O. Gunnarsson, *Rep. Prog. Phys.*, 1998, **61**, 237, DOI: 10.1088/0034-4885/61/3/002.
47 G. Onida, L. Reining and A. Rubio, *Rev. Mod. Phys.*, 2002, **74**, 601, DOI: 10.1103/RevModPhys.74.601.
48 E. Runge and E. K. U. Gross, *Phys. Rev. Lett.*, 1984, **52**, 997, DOI: 10.1103/PhysRevLett.52.997.
49 V. Olevano, TDDFT, excitations, and spectroscopy, in *Structures on Different Time Scales*, ed. T. Woike and D. Schaniel, Walter de Gruyter GmbH, Berlin, 2018, pp. 101–142.
50 Ph. Ghosez, X. Gonze and R. W. Godby, *Phys. Rev. B: Condens. Matter Mater. Phys.*, 1997, **56**, 12811, DOI: 10.1103/PhysRevB.56.12811.
51 Z.-h. Yang and C. A. Ullrich, *Phys. Rev. B: Condens. Matter Mater. Phys.*, 2013, **87**, 195204, DOI: 10.1103/PhysRevB.87.195204.
52 S. Sharma, J. K. Dewhurst, S. Shallcross, G. K. Madjarova and E. K. U. Gross, *J. Chem. Theory Comput.*, 2015, **11**, 1710, DOI: 10.1021/acs.jctc.5b00133.
53 A. Zangwill and P. Soven, *Phys. Rev. A*, 1980, **21**, 1561, DOI: 10.1103/PhysRevA.21.1561.
54 E. K. U. Gross, J. F. Dobson and M. Petersilka, Density Functional Theory of time-dependent phenomena, in *Density Functional Theory II: Relativistic and Time Dependent Extensions*, ed. R. F. Nalewajski, Springer, Berlin, 1996, pp. 81–172, DOI: 10.1007/BFb0016643.
55 L. Reining, V. Olevano, A. Rubio and G. Onida, *Phys. Rev. Lett.*, 2002, **88**, 066404, DOI: 10.1103/PhysRevLett.88.066404.
56 S. Sharma, J. K. Dewhurst, A. Sanna and E. K. U. Gross, *Phys. Rev. Lett.*, 2011, **107**, 186401, DOI: 10.1103/PhysRevLett.107.186401.
57 J. L. Lyons, J. B. Varley, E. R. Glaser, J. A. Freitas, J. C. Culbertson, F. Tian, G. A. Gamage, H. Sun, H. Ziyaee and Z. Ren, *Appl. Phys. Lett.*, 2018, **113**, 251902, DOI: 10.1063/1.5058134.
58 T. L. Chu and A. E. Hyslop, *J. Appl. Phys.*, 1972, **43**, 276, DOI: 10.1063/1.1661106.
59 B. Lv, Y. Lan, X. Wang, Q. Zhang, Y. Hu, A. J. Jacobson, D. Broido, G. Chen, Z. Ren and C.-W. Chu, *Appl. Phys. Lett.*, 2015, **106**, 074105, DOI: 10.1063/1.4913441.
60 X. Chen, C. Li, Y. Xu, A. Dolocan, G. Seward, A. V. Roekeghem, F. Tian, J. Xing, S. Guo, N. Ni, *et al.*, *Chem. Mater.*, 2021, **33**, 6974, DOI: 10.1021/acs.chemmater.1c02006.
61 L. Craco, S. S. Carara, E. da Silva Barboza, M. V. Milošević and T. A. S. Pereira, *RSC Adv.*, 2023, **13**, 17907, DOI: 10.1039/D3RA00898C.
62 S. Yue, F. Tian, B. Song, Y. Zhong, J. Bao and X. Liu, *Matter*, 2025, **8**, 102131, DOI: 10.1016/j.matt.2025.102131.
63 R. Resta and A. Baldereschi, *Phys. Rev. B: Condens. Matter Mater. Phys.*, 1981, **23**, 6615, DOI: 10.1103/PhysRevB.23.6615.
64 J. C. Phillips, *Rev. Mod. Phys.*, 1970, **42**, 317, DOI: 10.1103/RevModPhys.42.317.
65 N. Joshi, V. Maurya and K. B. Joshi, *J. Phys.: Condens. Matter*, 2023, **35**, 215901, DOI: 10.1088/1361-648X/acc378.
66 N. Joshi, V. Maurya and K. B. Joshi, *Solid State Commun.*, 2023, **371**, 115290, DOI: 10.1016/j.ssc.2023.115290.
67 N. Joshi, S. Jangir, S. Sharma, V. Maurya and K. B. Joshi, *Phys. Scr.*, 2024, **99**, 115981, DOI: 10.1088/1402-4896/ad8274.
68 S. Jangir, N. Joshi and K. B. Joshi, *J. Appl. Phys.*, 2025, **138**, 043103, DOI: 10.1063/5.0274074.
69 S. Sharma, J. K. Dewhurst and E. K. U. Gross, Optical Response of Extended Systems Using Time-Dependent Density Functional Theory, in *First Principles Approaches to Spectroscopic Properties of Complex Materials*, ed. C. Di Valentin, S. Botti and M. Cococcioni, Springer, Berlin, 2014, pp. 235–257, DOI: 10.1007/128_2014_529.
70 Z. Ning, C.-T. Liang and Y.-C. Chang, *Phys. Rev. B*, 2017, **96**, 085202, DOI: 10.1103/PhysRevB.96.085202.
71 Y.-M. Byun, J. Sun and C. A. Ullrich, *Electron. Struct.*, 2020, **2**, 023002, DOI: 10.1088/2516-1075/ab7b12.
72 S. Botti, A. Fourreau, F. Nguyen, Y.-O. Renault, F. Sottile and L. Reining, *Phys. Rev. B: Condens. Matter Mater. Phys.*, 2005, **72**, 125203, DOI: 10.1103/PhysRevB.72.125203.
73 S. Botti, F. Sottile, N. Vast, V. Olevano, L. Reining, H. – C. Weissker, A. Rubio, G. Onida, R. Del Sole and R. W. Godby, *Phys. Rev. B: Condens. Matter Mater. Phys.*, 2004, **69**, 155112, DOI: 10.1103/PhysRevB.69.155112.
74 C. A. Ullrich and Z.-h. Yang, *Braz. J. Phys.*, 2014, **44**, 154, DOI: 10.1007/s13538-013-0141-2.
75 F. Aryasetiawan and O. Gunnarsson, *Phys. Rev. B: Condens. Matter Mater. Phys.*, 2002, **66**, 165119, DOI: 10.1103/PhysRevB.66.165119.
76 P. E. Trevisanutto, A. Terentjevs, L. A. Constantin, V. Olevano and F. D. Sala, *Phys. Rev. B: Condens. Matter Mater. Phys.*, 2013, **87**, 205143, DOI: 10.1103/PhysRevB.87.205143.
77 S. Waidmann, M. Knupfer, B. Arnold, J. Fink, A. Fleszar and W. Hanke, *Phys. Rev. B: Condens. Matter Mater. Phys.*, 2000, **61**, 10149, DOI: 10.1103/PhysRevB.61.10149.
78 L. K. Dash, N. Vast, P. Baranek, M.-C. Cheynet and L. Reining, *Phys. Rev. B: Condens. Matter Mater. Phys.*, 2004, **70**, 245116, DOI: 10.1103/PhysRevB.70.245116.
79 F. Sottile, F. Bruneval, A. G. Marinopoulos, L. K. Dash, S. Botti, V. Olevano, N. Vast, A. Rubio and L. Reining, *Int. J. Quantum Chem.*, 2005, **102**, 684, DOI: 10.1002/qua.20486.
80 Y.-M. Byun and C. A. Ullrich, *Phys. Rev. B*, 2017, **95**, 205136, DOI: 10.1103/PhysRevB.95.205136.
81 A. V. Terentjev, L. A. Constantin and J. M. Pitarke, *Phys. Rev. B*, 2018, **98**, 085123, DOI: 10.1103/PhysRevB.98.085123.
82 V. Olevano and L. Reining, *Phys. Rev. Lett.*, 2001, **86**, 5962, DOI: 10.1103/PhysRevLett.86.5962.

83 A. Alkauskas, S. D. Schneider, S. Sagmeister, C. Ambrosch-Draxl and C. Hébert, *Ultramicroscopy*, 2010, **110**, 1081, DOI: 10.1016/j.ultramic.2009.12.004.
84 R. F. Egerton, *Electron Energy-Loss Spectroscopy in the Electron Microscope*, Springer, New York, 2011.
85 I. Timrov, N. Vast, R. Gebauer and S. Baroni, *Comput. Phys. Commun.*, 2015, **196**, 460, DOI: 10.1016/j.cpc.2015.05.021.
86 J. R. Chelikowsky and M. L. Cohen, *Phys. Rev. B*, 1976, **14**, 556, DOI: 10.1103/PhysRevB.14.556.
87 V. Vyas, V. Purvia, Y. C. Sharma, K. B. Joshi and B. K. Sharma, *Phys. Status Solidi B*, 2006, **243**, 1253, DOI: 10.1002/pssb.200541462.
88 P. Vogl, *J. Phys. C: Solid State Phys.*, 1978, **11**, 251, DOI: 10.1088/0022-3719/11/2/011.
89 M. Arruabarrena, A. Leonardo and A. Ayuela, *Phys. Rev. B*, 2023, **108**, 235210, DOI: 10.1103/PhysRevB.108.235210.
90 M. L. Cohen and T. K. Bergstresser, *Phys. Rev.*, 1966, **141**, 789, DOI: 10.1103/PhysRev.141.789.
91 *The Elk Code, version 6.3.02*, https://elk.sourceforge.net/.
92 D. J. Singh and L. Nordström, *Planewaves, Pseudopotentials, and the LAPW Method*, Springer, New York, 2006, DOI: 10.1007/978-0-387-29684-5_5.
93 J. P. Perdew and A. Zunger, *Phys. Rev. B: Condens. Matter Mater. Phys.*, 1981, **23**, 5048, DOI: 10.1103/PhysRevB.23.5048.
94 H. J. Monkhorst and J. D. Pack, *Phys. Rev. B*, 1976, **13**, 5188, DOI: 10.1103/PhysRevB.13.5188.
95 G. P. Srivastava, *J. Phys. A: Math. Gen.*, 1984, **17**, L317, DOI: 10.1088/0305-4470/17/6/002.
96 F. D. Murnaghan, *Proc. Natl. Acad. Sci. U. S. A.*, 1944, **30**, 244, DOI: 10.1073/pnas.30.9.244.
97 B. Arnaud and M. Alouani, *Phys. Rev. B: Condens. Matter Mater. Phys.*, 2001, **63**, 085208, DOI: 10.1103/PhysRevB.63.085208.
98 R. W. Godby, M. Schlüter and L. J. Sham, *Phys. Rev. B: Condens. Matter Mater. Phys.*, 1988, **37**, 10159, DOI: 10.1103/PhysRevB.37.10159.
99 F. Nastos, B. Olejnik, K. Schwarz and J. E. Sipe, *Phys. Rev. B: Condens. Matter Mater. Phys.*, 2005, **72**, 045223, DOI: 10.1103/PhysRevB.72.045223.
100 J. Da Ng and A. Danner, *Phys. Scr.*, 2021, **96**, 055801, DOI: 10.1088/1402-4896/abe0f1.
101 R. Markowski, M. Piacentini, D. Debowska, M. Zimnal-Starnawska, F. Lama, N. Zema and A. Kisiel, *J. Phys.: Condens. Matter*, 1994, **6**, 3207, DOI: 10.1088/0953-8984/6/17/010.
102 Y. Al-Douri, H. Abid, A. Zaoui and H. Aourag, *Phys. B*, 2001, **301**, 295, DOI: 10.1016/S0921-4526(01)00258-7.
103 C. B. Swarnkar, R. K. Pandya, U. Paliwal, N. N. Patel and K. B. Joshi, *Chalcogenide Lett.*, 2009, **6**, 137.
104 D. Azhikodan, S. Sharma and T. Nautiyal, *AIP Conf. Proc.*, 2015, **1665**, 120040, DOI: 10.1063/1.4918147.
105 S. Ozaki and S. Adachi, *Phys. Rev. B: Condens. Matter Mater. Phys.*, 2001, **64**, 085208, DOI: 10.1103/PhysRevB.64.085208.
106 G. A. Samara, *Phys. Rev. B: Condens. Matter Mater. Phys.*, 1983, **27**, 3494, DOI: 10.1103/PhysRevB.27.3494.
107 R. H. Lyddane, R. G. Sachs and E. Teller, *Phys. Rev.*, 1941, **59**, 673, DOI: 10.1103/PhysRev.59.673.
108 A. J. Sievers and J. B. Page, *Infrared Phys.*, 1991, **32**, 425, DOI: 10.1016/0020-0891(91)90130-8.
109 T.-H. Liu, B. Song, L. Meroueh, Z. Ding, Q. Song, J. Zhou, M. Li and G. Chen, *Phys. Rev. B*, 2018, **98**, 081203(R), DOI: 10.1103/PhysRevB.98.081203.
110 F. Naccarato, F. Ricci, J. Suntivich, G. Hautier, L. Wirtz and G.-M. Rignanese, *Phys. Rev. Mater.*, 2019, **3**, 044602, DOI: 10.1103/PhysRevMaterials.3.044602.
111 H. Mendlowitz, *J. Opt. Soc. Am.*, 1960, **50**, 739, DOI: 10.1364/JOSA.50.000739.
112 Z. Usman, C. Cao, G. Nabi, D. Y. Kun, W. S. Khan, T. Mehmood and S. Hussain, *J. Phys. Chem. A*, 2011, **115**, 6622, DOI: 10.1021/jp201495e.
113 V. J. Keast, *J. Electron Spectrosc. Relat. Phenom.*, 2005, **143**, 97, DOI: 10.1016/j.elspec.2004.04.005.
114 L. Hung, C. Guedj, N. Bernier, P. Blaise, V. Olevano and F. Sottile, *Phys. Rev. B*, 2016, **93**, 165105, DOI: 10.1103/PhysRevB.93.165105.
115 E. Moynihan, S. Rost, E. O'Connell, Q. Ramasse, C. Friedrich and U. Bangert, *J. Microsc.*, 2020, **279**, 256, DOI: 10.1111/jmi.12900.
116 S. Botti, A. Schindlmayr, R. F. Del Sole and L. Reining, *Rep. Prog. Phys.*, 2007, **70**, 357, DOI: 10.1088/0034-4885/70/3/R02.
117 P. Schattschneider, *Ultramicroscopy*, 1989, **28**, 1, DOI: 10.1016/0304-3991(89)90262-3.
118 P. Ravindran, A. Delin, R. Ahuja, B. Johansson, S. Auluck, J. M. Wills and O. Eriksson, *Phys. Rev. B: Condens. Matter Mater. Phys.*, 1997, **56**, 6851, DOI: 10.1103/PhysRevB.56.6851.